Size matters: abundance matching, galaxy sizes, and the Tully–Fisher relation in EAGLE

Ismael Ferrero,[1,2]★ Julio F. Navarro,[3]† Mario G. Abadi,[1,2] Laura V. Sales,[4] Richard G. Bower,[5] Robert A. Crain,[6]‡ Carlos S. Frenk,[5] Matthieu Schaller,[5] Joop Schaye[7] and Tom Theuns[5]

[1]*Instituto de Astronomía Teórica y Experimental, CONICET-UNC, Laprida 854, X5000BGR, Córdoba, Argentina*
[2]*Observatorio Astronómico de Córdoba, Universidad Nacional de Córdoba, Laprida 854, X5000BGR, Córdoba, Argentina*
[3]*Department of Physics and Astronomy, University of Victoria, Victoria, BC V8P 5C2, Canada*
[4]*Department of Physics and Astronomy, University of California, Riverside, CA 92521, USA*
[5]*Institute for Computational Cosmology, Department of Physics, Durham University, South Road, Durham DH1 3LE, UK*
[6]*Astrophysics Research Institute, Liverpool John Moores University, 146 Brownlow Hill, Liverpool L3 5RF, UK*
[7]*Leiden Observatory, Leiden University, PO Box 9513, 2300 RA Leiden, the Netherlands*

ABSTRACT

The Tully–Fisher relation (TFR) links the stellar mass of a disc galaxy, M_{str}, to its rotation speed: it is well approximated by a power law, shows little scatter, and evolves weakly with redshift. The relation has been interpreted as reflecting the mass–velocity scaling ($M \propto V^3$) of dark matter haloes, but this interpretation has been called into question by abundance-matching (AM) models, which predict the galaxy–halo mass relation to deviate substantially from a single power law and to evolve rapidly with redshift. We study the TFR of luminous spirals and its relation to AM using the EAGLE set of Λ cold dark matter (ΛCDM) cosmological simulations. Matching both relations requires disc sizes to satisfy constraints given by the concentration of haloes and their response to galaxy assembly. EAGLE galaxies approximately match these constraints and show a tight mass–velocity scaling that compares favourably with the observed TFR. The TFR is degenerate to changes in galaxy formation efficiency and the mass–size relation; simulations that fail to match the galaxy stellar mass function may fit the observed TFR if galaxies follow a different mass–size relation. The small scatter in the simulated TFR results because, at fixed halo mass, galaxy mass and rotation speed correlate strongly, scattering galaxies along the main relation. EAGLE galaxies evolve with lookback time following approximately the prescriptions of AM models and the observed mass–size relation of bright spirals, leading to a weak TFR evolution consistent with observation out to $z = 1$. ΛCDM models that match both the abundance and size of galaxies as a function of stellar mass have no difficulty reproducing the observed TFR and its evolution.

Key words: Galaxy: formation – Galaxy: kinematics and dynamics – Galaxy: structure.

1 INTRODUCTION

The Tully–Fisher relation (TFR) links the luminosity of disc galaxies with their characteristic rotation speed. First noted by Tully & Fisher (1977) using photographic magnitudes and H I velocity widths, it has become one of the best-studied galaxy scaling relations and a powerful secondary distance indicator. It is well approximated, for luminous spirals, by a tight power law whose dependence on wavelength is fairly well understood (Aaronson, Huchra & Mould 1979; Mathewson, Ford & Buchhorn 1992; Tully et al. 1998; Haynes et al. 1999; Verheijen 2001; Courteau et al. 2007). As a result, the relation is now routinely cast in terms of galaxy stellar mass and the circular speed measured at a characteristic 'luminous radius' (Bell & de Jong 2001; Avila-Reese et al. 2008; Reyes et al. 2011). Since rotation curves are nearly flat, the choice of radius is not critical for luminous spirals, but popular choices include 2.2 times the exponential scalelength (e.g. Courteau 1997) or, alternatively, a radius that contains roughly 80 per cent of all stars (e.g. Pizagno et al. 2007).

The evolution of the TFR with redshift has been more difficult to pin down, although the consensus is that the TFR evolves weakly, if

at all, up to $z \approx 1$. Early studies, many of them in the *B* band, claimed significant evolution in either the zero-point, the slope or in both (e.g. Ziegler et al. 2002; Böhm et al. 2004), but these conclusions evolved once data on longer wavelengths less affected by extinction became available. Conselice et al. (2005) and Flores et al. (2006), for example, found no significant evolution in the *K*-band TFR to $z \approx 1.3$ and 0.6, respectively. This conclusion has been supported by the more recent work of Miller et al. (2011), who conclude that there is no substantial change in the stellar mass TFR out to redshifts of about unity. Observations at higher redshifts hint at more substantial evolution of the zero-point, although the presence of large random motions and selection effects at such early times complicate the interpretation (Cresci et al. 2009; Förster Schreiber et al. 2009; Kassin et al. 2012).

The properties of the TFR have long challenged direct numerical simulations of disc galaxy formation in the Λ cold dark matter (ΛCDM) scenario. Early work, for example, produced galaxies so massive and compact that their rotation curves were steeply declining and, at given galaxy mass, peaked at much higher velocities than observed (see e.g. Navarro & Steinmetz 2000; Abadi et al. 2003; Scannapieco et al. 2012, and references therein). The problem was quickly traced to the inability of early feedback schemes to prevent large amounts of low angular momentum baryons from accumulating early at the centre of dark matter haloes.

Subsequent work made progress by adopting feedback schemes able to remove a large fraction of the early-collapsing baryons and to regulate their further accretion, leading to discs with sizes and rotation curves in better accord with observation (e.g. Okamoto et al. 2005; Governato et al. 2007; Brook et al. 2011; McCarthy et al. 2012; Aumer et al. 2013; Guedes et al. 2013; Marinacci, Pakmor & Springel 2014). Although such results were promising, they were inconclusive, especially because they were either based on a handful of carefully selected, and therefore likely highly biased, individual systems, or on cosmological boxes where simulated galaxies failed to match basic statistics of the observed galaxy population, such as the galaxy stellar mass function.

As a result, much theoretical TFR work in the context of the ΛCDM cosmology has proceeded via semi-analytic models of galaxy formation. These models employ simple, albeit well founded, prescriptions to generate a synthetic galaxy population within an evolving population of dark matter haloes. The physical properties of such a population are then compared with observed galaxies in order to calibrate the assumed prescriptions and to shed light on to the role of various mechanisms during galaxy formation. Semi-analytic models have highlighted a number of difficulties, particularly when attempting to match simultaneously the abundance of galaxies as a function of stellar mass and the slope and normalization of the TFR (see e.g. Cole et al. 2000; Dutton et al. 2010, and references therein). Some of these difficulties may be traced to the adoption of incorrect cosmological parameters, to the use of simple but likely biased proxies for the disc rotation speed, such as the maximum circular velocity of the halo, or to uncertainties in the halo response to galaxy assembly. Recent attempts, where these issues have been improved upon, report much better agreement (see e.g. Desmond & Wechsler 2015; Lacey et al. 2016).

The basic reason for these difficulties is that these models generally (and reasonably) assign more massive galaxies to more massive haloes, leading to a tight relation between galaxy and halo masses that place strong constraints on their characteristic circular speed. A simple model for this galaxy–halo mass relation may be derived by ranking galaxies by mass and assigning them to haloes ranked in similar fashion, preserving the ranked order (Frenk et al. 1988;

Vale & Ostriker 2004; Guo et al. 2010; Behroozi et al. 2013; Moster, Naab & White 2013). This 'abundance-matching' (AM) exercise has proven particularly useful when assessing the results of numerical simulations, especially those of single isolated systems, where there is otherwise little guidance about the mass or size of the galaxy that may form in one particular halo.

Since the dark mass profile of ΛCDM haloes is well known (Navarro, Frenk & White 1996, 1997), AM models have little freedom left when trying to match the TFR: a galaxy's characteristic circular velocity is fixed once its radius and the halo response have been specified (see e.g. Cattaneo, Salucci & Papastergis 2014). The critical role of galaxy size and halo response implies that insight into the origin of the TFR requires a good understanding of the interplay between galaxies' mass and size, as well as of the mass of the haloes they inhabit and how galaxies might modify them.

These complex issues are best studied through cosmological hydrodynamical simulations, especially those able to follow statistically significant numbers of galaxies over large volumes, and to resolve their inner regions, where rotation speeds are measured. These conditions are well met by the latest round of cosmological hydrodynamical simulations, such as the recently completed Illustris and EAGLE projects (Vogelsberger et al. 2013; Schaye et al. 2015). One main conclusion from these efforts is that, except for the lowest masses (Sawala et al. 2013, 2015), AM predictions are actually quite robust: matching the observed galaxy stellar mass function requires simulations to reproduce accurately the galaxy–halo mass relation envisioned by AM models, with little scatter.

One intriguing result, however, is that both Illustris and EAGLE report good agreement with the observed TFR, despite the fact that the galaxy stellar mass functions they report differ significantly. This approximate 'invariance' of the simulated TFR has been noted in the past. Guo et al. (2010), for example, found that a number of simulated galaxies, which in earlier work had been reported to match the TFR, actually had masses that greatly exceeded AM predictions. A similar result has been discussed recently by Torrey et al. (2014), who showed that the TFR in their simulations is insensitive to large variations in the Illustris galaxy formation physics submodules: only models with 'no feedback' were found to be in substantial disagreement with the observed TFR. Although Torrey et al. (2014) cite 'feedback' as an essential ingredient to match the TFR, its actual role in determining its slope and zero-point remains unclear, a point underlined by the recent results of Crain et al. (2015), who report that the TFR is actually quite sensitive to feedback, at least in their implementation.

We examine these issues here using the EAGLE set of ΛCDM cosmological hydrodynamical simulations. We analyse the stellar mass TFR in the regime of luminous spirals, where gas contributes little to the overall baryon budget, and report results on the baryonic TFR of gas-dominated, fainter galaxies in a separate paper (Sales et al. 2016). We pay particular attention to the effect of galaxy sizes on the TFR, an issue that has been relatively well explored in semi-analytic approaches but that has received little attention in direct simulation TFR work.

We begin in Section 2 by motivating the effect of galaxy size on the TFR by simple considerations that highlight the need for halo contraction in order to reconcile the TFR with the predictions of AM models. We then present, in Section 3, the TFR of simulated galaxies in EAGLE, with particular attention to the origin of its small scatter (Section 3.4) and its evolution (Section 3.5). We conclude with a brief summary of our main findings in Section 4.
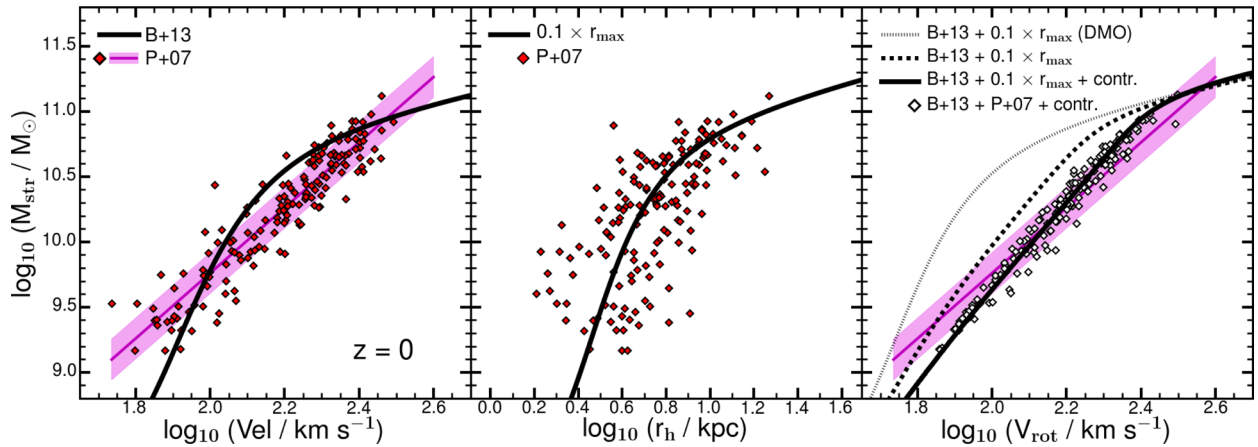
Figure 1. Galaxy stellar mass, M_{str}, as a function of various parameters. Left: the solid black curve shows the AM prediction of Behroozi et al. (2013, B+13), as a function of halo virial velocity, V_{200}. Symbols correspond to the data of Pizagno et al. (2007, P+07), converted to stellar masses using a constant *I*-band mass-to-light ratio of 1.2 (Bell et al. 2003) and shown as a function of disc rotation speed, V_{rot}. Colour-shaded band indicates the mean slope and 1σ scatter. Middle: symbols show half-light radii of galaxies in the P+07 sample. Thick solid line indicates a multiple of r_{max}, the characteristic radius where NFW halo circular velocities peak. Halo masses are as in the B+13 model of the left-hand panel. Right: TFR. The colour band is the same as in the left-hand panel. The dotted curve indicates the dark halo circular velocity at $r_h = 0.1\,r_{max}$, assuming NFW profiles and neglecting the contribution of the disc. The dashed line includes the gravitational contribution of the disc, keeping the halo unchanged. Finally, the thick solid line (and symbols) includes the disc contribution and assumes that haloes contract adiabatically.

2 TULLY–FISHER, ABUNDANCE MATCHING, AND GALAXY SIZES

In a cosmological context, the TFR has often been thought to reflect the equivalence between halo mass and circular velocity imposed by the finite age of the Universe (see e.g. Mo, Mao & White 1998; Steinmetz & Navarro 1999). That characteristic time-scale translates into a fixed density contrast which implies a scaling between virial[1] mass and circular velocity given by

$$M_{200} = \frac{V_{200}^3}{10\,G\,H(z)}, \tag{1}$$

where G is the gravitational constant and $H(z)$ is the Hubble constant. The power-law scaling resembles the TFR, provided that galaxy masses and rotation velocities scale roughly in proportion to the virial masses and circular velocities of the haloes they inhabit (Navarro & Steinmetz 2000).

This interpretation, however, is difficult to reconcile with AM arguments, which suggest that galaxy masses are not simply proportional to the virial mass of the halo they inhabit. Indeed, AM models require the 'galaxy formation efficiency', $f_m \equiv M_{str}/M_{200}$, to be a non-monotonic function of virial mass, reaching a maximum at $M_{200} \sim 10^{12}\,M_\odot$ and declining steeply towards lower and higher masses (e.g. Eke et al. 2005; Guo et al. 2010; Behroozi et al. 2013; Moster et al. 2013). In addition, galaxy formation efficiencies evolve relatively rapidly in AM models, in contrast with the weak evolution of the TFR discussed in Section 1. A simple proportionality between the mass and velocity of galaxies and haloes is thus clearly inadequate to explain the TFR within the context of AM models.

We show this in the left-hand panel of Fig. 1, where the solid black curve indicates the relation between M_{str}, the stellar mass of a galaxy, and V_{200}, the circular velocity of its halo, according to the

model of Behroozi et al. (2013, hereafter, B+13). For comparison, the red symbols show the Tully–Fisher data from the sample of Pizagno et al. (2007, hereafter, P+07). This comparison shows that reconciling AM predictions with the TFR requires the relation between disc rotation speed, V_{rot}, and halo virial velocity to be non-monotonic: rotation speeds must underestimate or overestimate halo circular velocities, depending on M_{str}. In other words, if f_m is non-monotonic, then the ratio $f_v \equiv V_{rot}/V_{200}$ cannot be monotonic either (see Cattaneo et al. 2014, for a similar analysis).

Rotation speeds are set by the total (dark plus luminous) mass enclosed within a given radius, so the ratio f_v depends sensitively on galaxy size: in general, at given M_{str}, the smaller the galaxy the larger the contribution of the disc to V_{rot} and the lesser the importance of the dark halo. Quantitatively, the result depends on the density profile of the halo and on its response to the assembly of the galaxy.

It is instructive to consider each effect separately. We begin by noting that the half-light radii, r_h, of galaxies in the P+07 sample (shown in the middle panel of Fig. 1) are well approximated by a simple multiple of r_{max}, the characteristic radius where ΛCDM haloes reach their peak circular velocity, V_{max}. This means that, if the luminous component was unimportant, disc rotation speeds, identified with the circular velocity at r_h, would be just a multiple of the virial velocity. This is shown by the dotted curve in the right-hand panel of Fig. 1, where we have assumed that haloes follow an NFW profile (Navarro et al. 1996, 1997) with concentrations given by the $M_{200}-c$ relation derived from the latest set of large cosmological *N*-body simulations (Ludlow et al. 2016, their appendix C). Clearly, this provides a rather poor match to the observed TFR.

Simply adding in quadrature, the velocity contribution of the luminous galaxy (keeping the haloes unchanged) tilts and shifts the relation to that indicated by the thick dashed curve in the same panel. The tilt in slope results because the gravitational importance of the disc (within r_h) increases with increasing M_{str}. The predicted rotation velocities are, however, still below observed values, suggesting that, if AM predictions hold, halo contraction is needed to explain the observed TFR.

[1] Virial quantities are identified by a '200' subscript and measured at the virial radius, r_{200}, defined as the radius where the enclosed mean density is 200 times the critical density of the Universe, $\rho_{crit} = 3H^2(z)/8\pi G$.

Modelling the halo response as 'adiabatic contraction' (Barnes & White 1984; Blumenthal et al. 1986) yields the individual symbols and the thick solid curve in the right-hand panel of Fig. 1. The contraction assumes that each spherical shell conserves $r\,V_c(r)$, where r is the radius and $V_c(r)$ its corresponding circular velocity (see e.g. the discussion of fig. 8 in Abadi et al. 2010). Contraction compounds the gravitational effect of the disc, tilting and shifting the relation further, and leading to a reasonably good agreement with the observed TFR, despite the simplicity of the model and the fact that we have not allowed for any adjustment or scatter in the AM prediction or in the mass–concentration relation. Note that the curvature in the mass–velocity relation characteristic of AM models is shifted to large velocities, where there is little data, resulting in a TFR that can be adequately approximated by a single power law with little scatter.

These results suggest that ΛCDM models should be able to match the observed TFR, *provided* that galaxy sizes are well reproduced, and that haloes respond roughly adiabatically to galaxy assembly. In particular, much smaller galaxy sizes would lead to excessively high rotation velocities at given galaxy mass, the main reason for the failure of early disc galaxy formation simulations discussed in Section 1. This discussion also illustrates that the TFR is a sensitive probe not only of the galaxy–halo mass relation, but also of galaxy sizes: indeed, models that deviate from the AM predictions may still fit the TFR if galaxy sizes are adjusted appropriately. We explore next whether these simple insights hold when analysing the TFR and its redshift evolution in a large cosmological hydrodynamical simulation.

3 NUMERICAL RESULTS

3.1 The EAGLE simulation

We use here the EAGLE[2] set of cosmological hydrodynamical simulations. We briefly summarize the main relevant aspects of these simulations and refer the interested reader to Schaye et al. (2015) for further details.

EAGLE used a heavily modified version of GADGET-3, an itself-modified version of the Tree-SPH hydrodynamical code GADGET-2 (Springel 2005). The modifications to the hydrodynamics solver are described and their effects investigated in Schaller et al. (2015b).The simulation includes subgrid models for radiative cooling (Wiersma, Schaye & Smith 2009a), star formation (Schaye & Dalla Vecchia 2008), stellar mass loss (Wiersma et al. 2009b), energetic feedback from star formation (Dalla Vecchia & Schaye 2012), black hole accretion, merging and feedback (Rosas-Guevara et al. 2015; Schaye et al. 2015; Springel 2005). The simulation assumes a ΛCDM cosmology with parameters consistent with the latest CMB experiments (Planck Collaboration I 2014): $\Omega_b = 0.0482$, $\Omega_{dark} = 0.2588$, $\Omega_\Lambda = 0.693$, and $h = 0.6777$, where $H_0 = 100\,h\,\mathrm{km\,s^{-1}\,Mpc^{-1}}$.

The simulation analysed here is referred to as Ref-L100N1504 in table 1 of Schaye et al. (2015). It follows 2×1504^3 particles in a periodic cubic volume of 100 Mpc on a side from redshift $z = 127$ to 0. This corresponds to an equal number of gas and dark matter particles with initial mass of $m_{gas} = 1.81 \times 10^6\,\mathrm{M_\odot}$ and $m_{DM} = 9.70 \times 10^6\,\mathrm{M_\odot}$ per particle. The simulation uses a Plummer-equivalent gravitational softening of $\epsilon = 2.66$ kpc (comoving units) before redshift $z = 2.8$ and fixed at $\epsilon = 0.7$ kpc (physical units) after that. The numerical parameters in the EAGLE

subgrid physics modules for feedback have been calibrated to the observed $z = 0$ galaxy stellar mass function and the distribution of galaxy sizes.

Schaye et al. (2015) have presented a preliminary version of the TFR using the maximum circular velocity as a proxy for the disc rotation speeds. Crain et al. (2015) have also analysed the TFR, especially its dependence on feedback strength; they report an increase in rotation speed at fixed mass when feedback is more efficient (see their fig. 10d). Our analysis extends this work by focusing on velocities measured at the half-mass radii of the simulated galaxies (closer to what is actually observed), by considering the importance of galaxy sizes, and by examining the evolution of the TFR with redshift.

3.2 The simulated galaxy sample

Galaxies are identified in EAGLE using the SUBFIND algorithm (Springel, Yoshida & White 2001; Dolag et al. 2009), which selects gravitationally bound substructures (subhaloes) in haloes found by a friends-of-friends (FoF) algorithm with linking length 0.2 times the mean interparticle separation (Davis et al. 1985). The centre of each subhalo is defined as the position of the member particle with the minimum gravitational potential energy. Galaxy properties are computed within a 'galaxy radius' defined by the smaller of either $r_{gal} = 0.15\,r_{200}$ or 50 kpc, a choice that encompasses most of the stars in each halo, as well as the majority of its cold gas.

We focus here on 'central' galaxies (i.e. those corresponding to the most massive subhalo in each FoF group) with a minimum stellar mass of $M_{str} = 10^9\,\mathrm{M_\odot}$ (i.e. about 700 star particles). We shall show results for all galaxies, as well as for 'disc' galaxies, defined as those whose rotational-to-total kinetic energy parameter $\kappa_{rot} = \Sigma V_{xy}^2 / \Sigma V^2 > 0.6$ (Sales et al. 2012). (Here V is the magnitude of the total velocity vector and $V_{xy} = j_z/R$ its azimuthal component perpendicular to the z direction, which is defined by the total angular momentum of the galaxy's stellar component.) Note that this criterion is quite strict, and selects only 11 per cent of all galaxies as discs at $z = 0$. Our final galaxy samples contain 7482 galaxies (867 of them discs) at $z = 0$, and 7922 galaxies (818 of them discs) at $z = 1$.

Fig. 2 shows the spatial distribution of the stellar component for three of our simulated disc galaxies, spanning a wide range of M_{str}, from $\sim 10^9$ to $10^{11}\,\mathrm{M_\odot}$. The three galaxies are shown face-on (top) and edge-on (middle), and have been chosen to have well-defined discs (i.e. $\kappa_{rot} > 0.6$). Their circular velocity curves, here approximated by $V_{circ}(r) = (GM(<r)/r)^{1/2}$, are shown in the bottom row and are approximately flat in the inner 10–30 kpc (Schaller et al. 2015a). Hereafter, we shall use the circular velocity at the stellar half-mass radius (shown by a dotted vertical line or circle in each panel) to define the characteristic rotation speed associated with each galaxy. Although formally, the circular velocity of an axisymmetric disc will differ from the definition provided above (which is correct for spherical systems), the corrections are typically smaller than 10 per cent. Therefore, for simplicity, we apply the same definition of circular velocity regardless of galaxy morphological type.

3.3 The simulated TFR

Fig. 3 summarizes the results of our simulation regarding AM, galaxy sizes, and the TFR at $z = 0$. The black solid curves are reproduced from Fig. 1, for ease of comparison. Individual simulated galaxies are shown in grey and disc galaxies in blue. In addition, all central galaxies in three narrow bins of halo mass are identified and highlighted in cyan, red, and orange to guide the discussion.
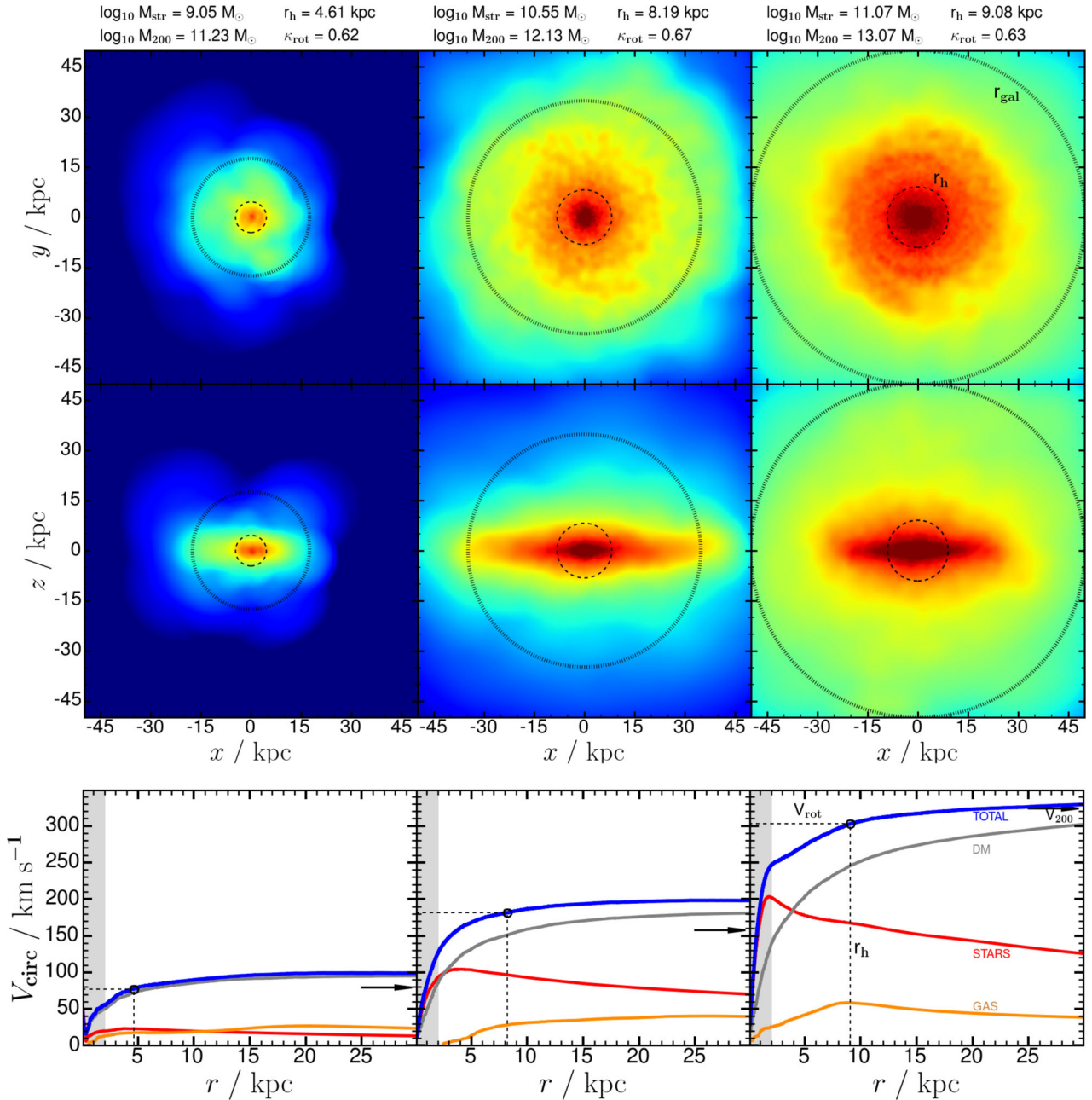
[2] http://eagle.strw.leidenuniv.nl

Figure 2. Stellar surface density maps of three simulated disc galaxies at $z = 0$. Stellar and halo masses, half-mass radii, and rotation parameter values are listed in the legends. The top row shows a face-on view of the discs, the middle row shows edge-on views. The inner and outer circles indicate stellar half-mass radii, r_h, and $r_{gal} = 0.15\, r_{200}$, respectively. The corresponding circular velocity curves are shown in the bottom row. Blue denotes total circular velocity, grey the dark matter contribution, red the stars and orange the gas. Stellar half-mass radii and rotation speeds, $V_{rot} = V_{circ}(r_h)$, are indicated by dotted lines. The halo virial velocity, V_{200}, is shown with a horizontal arrow in each bottom panel.

The leftmost panel shows that EAGLE follows the results of the B+13 AM model. The agreement is not perfect, however, and leads to slight but systematic deviations in the galaxy stellar mass function which, around its knee, is offset from the observational inferred relation by about a factor of 2. Discs follow the main galaxy mass–halo mass relation quite well, with a hint of higher-than-average galaxy formation efficiencies at fixed halo mass.

Simulated discs are also slightly larger than spheroids at given M_{str}, as shown in the middle panel of Fig. 3 (see Furlong et al. 2015a). The overall mass–size trend of simulated galaxies, however, is not far from that of the P+07 Tully–Fisher sample, as indicated by the solid black line, which is the same as in Fig. 1. There is, however,

a slight mismatch, which becomes evident at large masses, where EAGLE discs are smaller than in the observed sample, and at small masses, where the opposite is true.

Finally, the right-hand panel of Fig. 3 shows the simulated TFR, and compares it with the adiabatically contracted model of Fig. 1 (black solid line). The grey solid curve shows a fit of the form[3] $M_{str}/M_\odot = M_0\, \nu^\alpha \exp(-\nu^\gamma)$, where ν is the velocity in units of 50 km s^{-1}, $M_0 = 8.63 \times 10^8$, $\alpha = 4.1$ and $\gamma = 0.432$. The good

---

[3] This is the same fitting form proposed by Sales et al. (2016) to describe the simulated 'baryonic TFR' of APOSTLE and EAGLE galaxies.
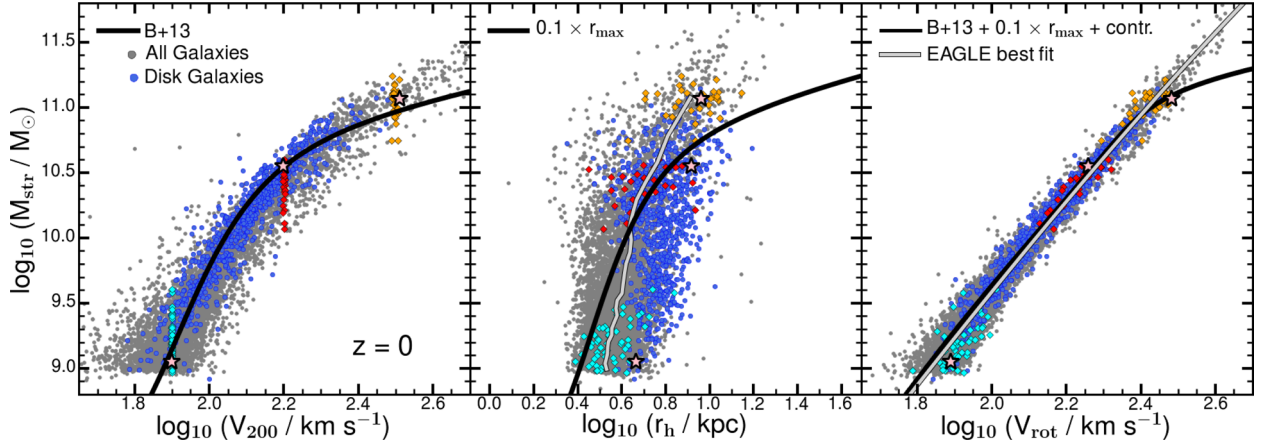
Figure 3. Analogous to Fig. 1, but for EAGLE galaxies at $z = 0$. Black solid lines are as in Fig. 1, and are included to aid comparison. Grey points correspond to all simulated galaxies, blue points indicate 'discs' according to a relatively strict criterion; i.e. systems with rotation parameter $\kappa_{rot} > 0.6$. Galaxies forming in three narrow bins of halo mass are highlighted in cyan, red, and orange. The three starred symbols indicate the three galaxies shown in the images of Fig. 2. Note that EAGLE galaxies: (i) follow closely the B+13 AM predictions (left), (ii) have sizes comparable to spirals in the TF sample of P+07 (middle); and (iii) have a TFR in good agreement with the predictions from the simple halo contraction model of Fig. 1 (right). The thin grey line is a fit to the simulated TFR; see parameters in Table 1.

Table 1. EAGLE best TFR fit parameters.

Redshift	$M_0 (\times 10^8)$	α	γ	σ_M (dex)	σ_V (dex)
0.00	8.63 ± 0.11	4.10 ± 0.05	0.432 ± 0.021	0.11	0.08
0.25	8.32 ± 0.12	4.13 ± 0.04	0.483 ± 0.016	0.10	0.07
0.75	6.60 ± 0.07	4.36 ± 0.03	0.594 ± 0.009	0.09	0.08
1.00	5.57 ± 0.06	4.46 ± 0.03	0.634 ± 0.008	0.09	0.08

Note. $M_{str}/M_{\odot} = M_0\, \nu^{\alpha} \exp(-\nu^{\gamma})$, where ν is the velocity in units of $50\,km\,s^{-1}$.

agreement between the grey and black curves suggests that the simple considerations discussed in Section 2 capture the basic ingredients of the relation between AM, galaxy sizes, and halo response seen in the EAGLE simulation.

Three points are worth emphasizing: (i) the TFR may be approximated by a single power law, and is much straighter than the AM mass–velocity relation; (ii) the TFR scatter is rather small, with an rms of 0.11 dex in mass, or 0.08 dex in velocity, and (iii) the TFR zero-point at $M_{str} = 10^{10}\,M_{\odot}$ (roughly the mid-point of the mass range considered here) is in excellent agreement with observation.

A more direct comparison with observation is shown in Fig. 4, where we plot the TFR for all EAGLE galaxies (shown by a grey band to illustrate the main relation $\pm 1\sigma$) together with data from five recent Tully–Fisher compilations.[4] EAGLE agrees with these data sets quite well, even when luminous early-type spirals from Williams, Bureau & Cappellari (2010) are added to the comparison. Note that the scatter in the simulated TFR is smaller than observed, even when considering *all galaxies*. Choosing only discs reduces the scatter even further, to ~0.09 dex in mass and 0.07 dex in velocity. We conclude that the EAGLE TFR is in excellent agreement with observations at $z = 0$. We extend this analysis to higher redshifts in Section 3.5, after exploring next what sets the slope, zero-point, and scatter of the simulated TFR.
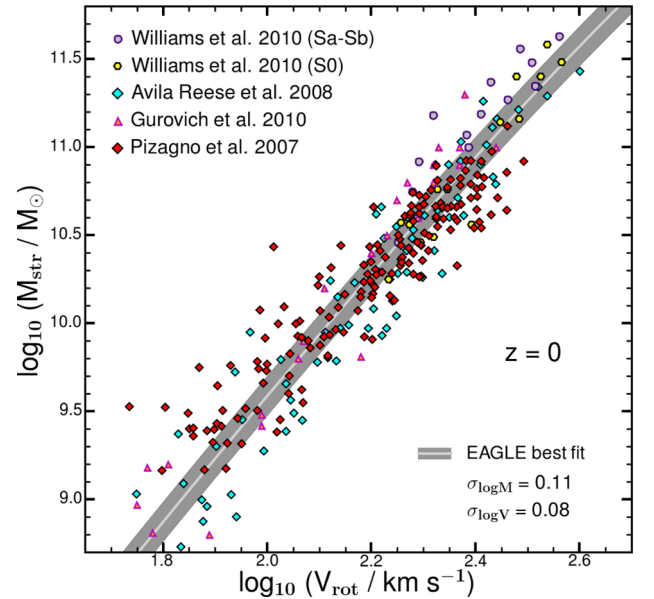

Figure 4. TFR for EAGLE galaxies (grey band) compared with individual spirals taken from five recent TF compilations. The simulated relation is in excellent agreement with the observational data. The scatter is even smaller than in observed samples, even though the simulated relation includes all galaxies and not only discs.

3.4 TFR slope, zero-point, and scatter

The TFR in ΛCDM is governed by the relation between galaxy formation efficiency, f_m, and the velocity ratio parameter, f_v, defined in Section 2. This is clear from equation (1), which may be re-written as

$$M_{str} = f_m M_{200} = \frac{f_m V_{200}^3}{10 G H(z)} = \frac{1}{10 G H(z)} \frac{f_m}{f_v^3} V_{rot}^3. \qquad (2)$$

The TFR is thus largely set by the ratio f_m/f_v^3: (i) its mass dependence determines the TFR slope; (ii) its actual value at some reference mass fixes the TFR zero-point; and (iii) its dispersion controls the TFR scatter. We explore these issues in more detail

---

[4] The observational data assume stellar masses derived assuming a Chabrier initial mass function (IMF). For galaxies in the Avila-Reese et al. (2008) compilation, we have reduced their published stellar masses by 0.15 dex in order to convert from Salpeter to Chabrier IMF.
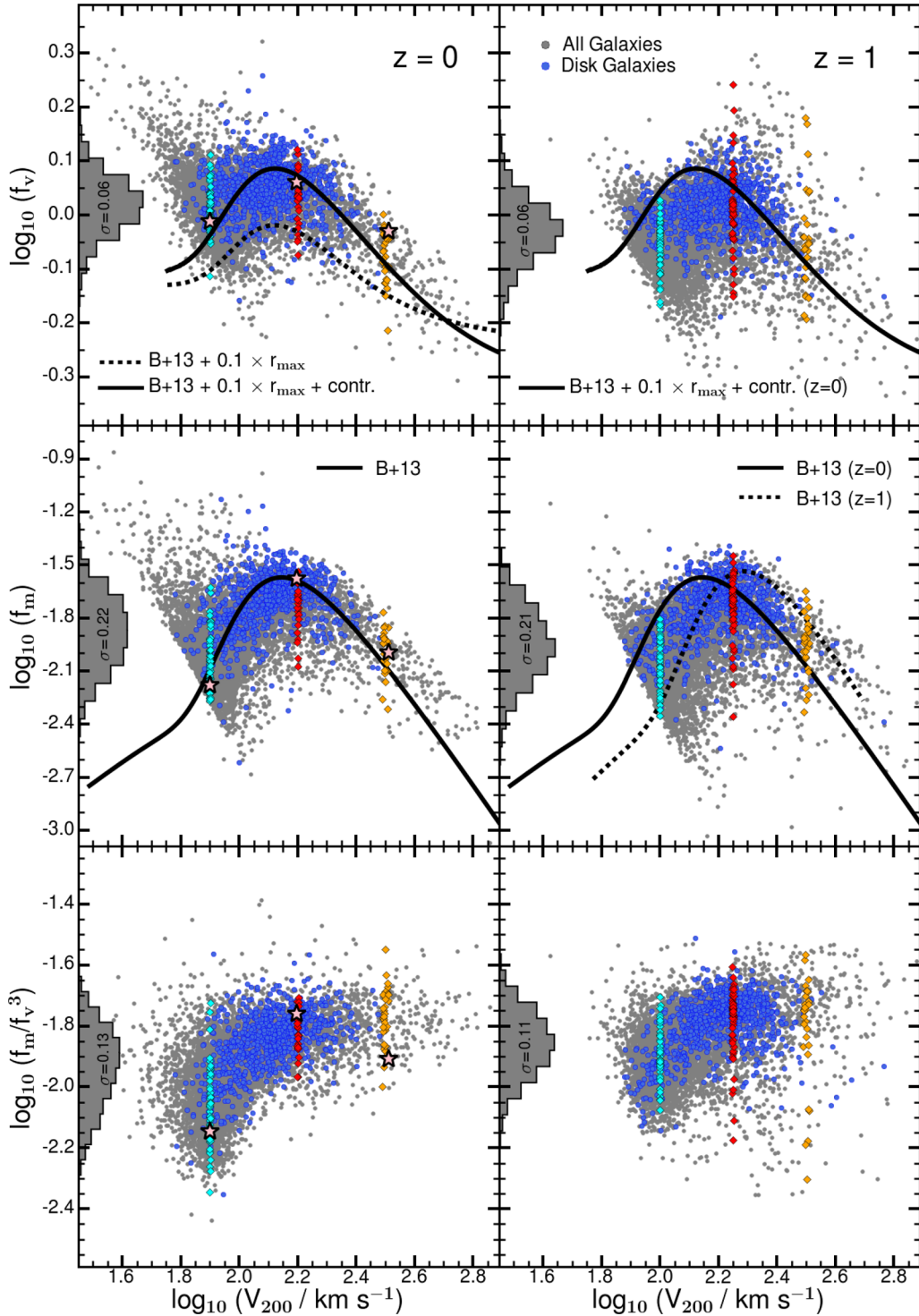
Figure 5. From top to bottom, the rows show, respectively, the velocity ratio parameter $f_v \equiv V_{\rm rot}/V_{200}$; the galaxy formation efficiency parameter, $f_m \equiv M_{\rm str}/M_{200}$; and the ratio f_m/f_v^3, as a function of virial velocity at $z = 0$ (left) and at $z = 1$ (right). Colours and symbols are as in Fig. 3. Solid curves correspond to the same model discussed in Fig. 1. The dashed curve in the f_v panel is the 'no contraction' case of Fig. 1.

in Fig. 5, where the left-hand panels show f_m, f_v, and f_m/f_v^3, as a function of halo virial velocity for EAGLE galaxies at $z = 0$.

Fig. 5 shows that, although f_m and f_v have a complex dependence on virial velocity, they are strongly correlated, resulting in a f_m/f_v^3 ratio that increases monotonically with halo mass. The monotonic

trend 'straightens' the resulting TFR into a single power law that matches observations.

The correlation between f_m and f_v is heavily dependent on galaxy sizes. Consider the solid line in the left-hand panel, f_v, of Fig. 5, which shows the result of applying the simple adiabatic contraction
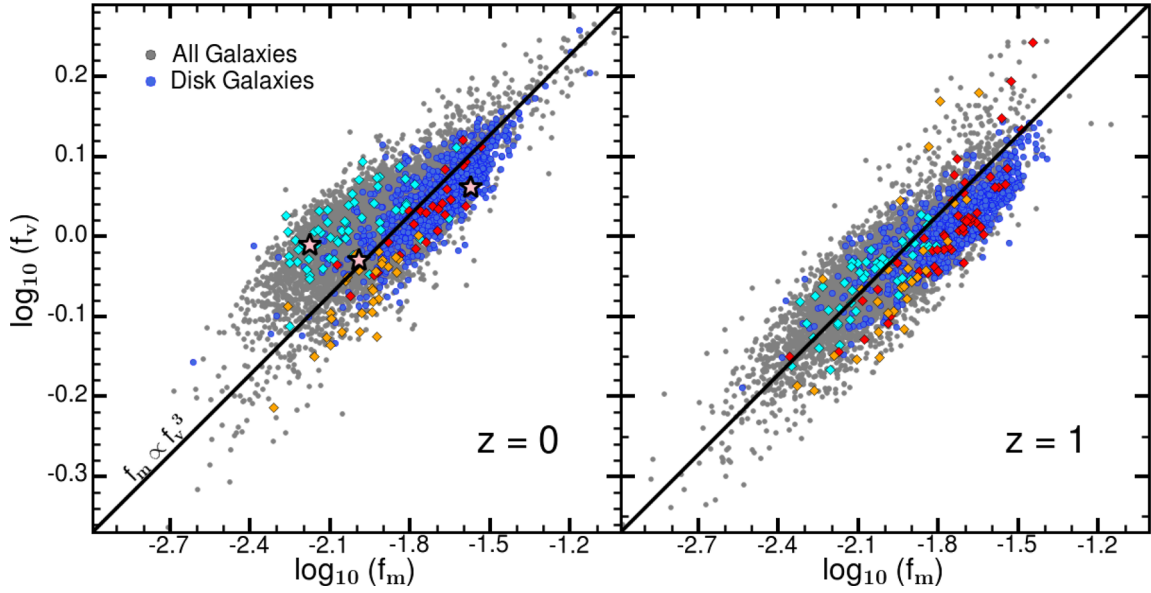
Figure 6. Correlation between the galaxy formation efficiency parameter $f_m \equiv M_{str}/M_{200}$, and the velocity ratio parameter, $f_v \equiv V_{rot}/V_{200}$, at $z = 0$ (left) and at $z = 1$ (right). Colours and symbols are as in Fig. 3. The relation $f_m \propto f_v^3$ is shown for reference as a straight solid line.

model of Fig. 1 to galaxies that satisfy the B+13 AM prescription, as well as the mass–size relation of the P+07 sample. The combination implies a non-monotonic mass dependence for f_v, resembling that of f_m. The magnitude of the effect on f_v depends on the actual sizes of the galaxies and on halo response. The 'no contraction' case is shown with a dashed curve. As discussed in Section 2, galaxy size and halo contraction play a crucial role in straightening the TFR into a power law.

We examine next the TFR zero-point by choosing, as reference, haloes with $V_{200} = 160\,\mathrm{km\,s^{-1}}$ (or 2.2 in $\log_{10}$ units). For such haloes, on average, $f_m = 0.02$ (set by AM) and $f_v = 1.08$ (set by size plus contraction); this implies $M_{str} = 2.7 \times 10^{10}\,\mathrm{M_\odot}$ at $V_{rot} = f_v V_{200} = 171\,\mathrm{km\,s^{-1}}$, in excellent agreement with observations, as judged from Fig. 4.

Finally, equation (2) shows that the TFR scatter depends on the dispersion in f_m/f_v^3 rather than on that in f_m or f_v, independently. Indeed, as discussed by Navarro & Steinmetz (2000), the surprisingly small scatter in the simulated TFR results from the strong mass–velocity correlation linking galaxies that form in haloes of the same virial mass.

This is clearly illustrated by the coloured dots in the right-hand panel of Fig. 3 which show that galaxies formed in haloes of fixed virial mass scatter along the main relation, compensating variations in galaxy formation efficiency with correlated changes in velocity. Such a correlation between f_m and f_v is expected, since, other things being equal, a disc mass increase will generally lead to a larger circular velocity. Quantitatively, the effect depends on the gravitational importance of the disc relative to that of the dark matter. Expressing this in terms of $\nu_{str} \equiv V_{str}/V_{dm}$; i.e. the ratio between the stellar and dark matter contributions to the circular velocity at r_h, $V_{rot} = (V_{str}^2 + V_{dm}^2)^{1/2}$, we can write

$$\delta \ln V_{rot} = \frac{1}{2} \frac{\nu_{str}^2}{(1 + \nu_{str}^2)} \delta \ln M_{str}. \qquad (3)$$

A change in galaxy mass, M_{str}, then induces a correlated change in velocity that is stronger the more important the disc is. For discs that contribute half of the total mass within the stellar half-mass radius ($\nu_{str} = 1$), we would then expect $f_m \propto f_v^4$, and $f_m \propto f_v^3$ for

systems as baryon dominated as $\nu_{str} = \sqrt{2}$. Although these trends neglect the effect of contraction, they account for the simulation results quite well, as may be seen from the f_m–f_v correlation shown in Fig. 6.

In other words, if discs are gravitationally important, then the TFR scatter is expected to be lower than the scatter in f_m or f_v alone. Baryons are indeed relatively important in EAGLE galaxies: at $z = 0$ their contribution increases steadily with mass/velocity, reaching about half of the mass within r_h for $V_{rot} = 150\,\mathrm{km\,s^{-1}}$. This leads to the strong correlation between f_m and f_v shown in Fig. 6 that drastically limits the scatter in the TFR: although the rms of f_m and f_v are 0.22 and 0.06 dex, respectively, that of the ratio f_m/f_v^3 is just 0.13 dex.

3.5 The evolution of the simulated TFR

According to the above discussion, the evolution of the TFR with redshift will depend critically on how galaxy formation efficiencies and sizes evolve with redshift. We present our results in Fig. 7 for three different redshifts: $z = 0.25$ (top row), 0.75 (middle row), and 1 (bottom row). Each row presents, as in Fig. 1, the galaxy–halo mass relation on the left, the galaxy mass–size relation in the middle, and the TFR in the rightmost panel. To guide the comparison, the solid black curves in each panel are the same as those shown in Fig. 1 for $z = 0$.

From top to bottom, the left-hand panels show that, at given V_{200}, EAGLE galaxy masses decrease with increasing redshift. This steady decrease in galaxy formation efficiency matches well that predicted by AM models, as shown by the dotted curves in each panel, taken from B+13. This is consistent with the agreement between the evolution of the simulated and observed galaxy mass function found by Furlong et al. (2015b). Note that the evolution in stellar mass is expected to be especially rapid at the low-mass end of the range studied here. At $V_{200} = 100\,\mathrm{km\,s^{-1}}$, for example, the stellar mass drops, according to B+13, by nearly an order of magnitude from $z = 0$ to $z = 1$.

Simulated galaxy sizes also evolve, as shown in the middle panels of Fig. 7. The evolution is especially noticeable at the massive
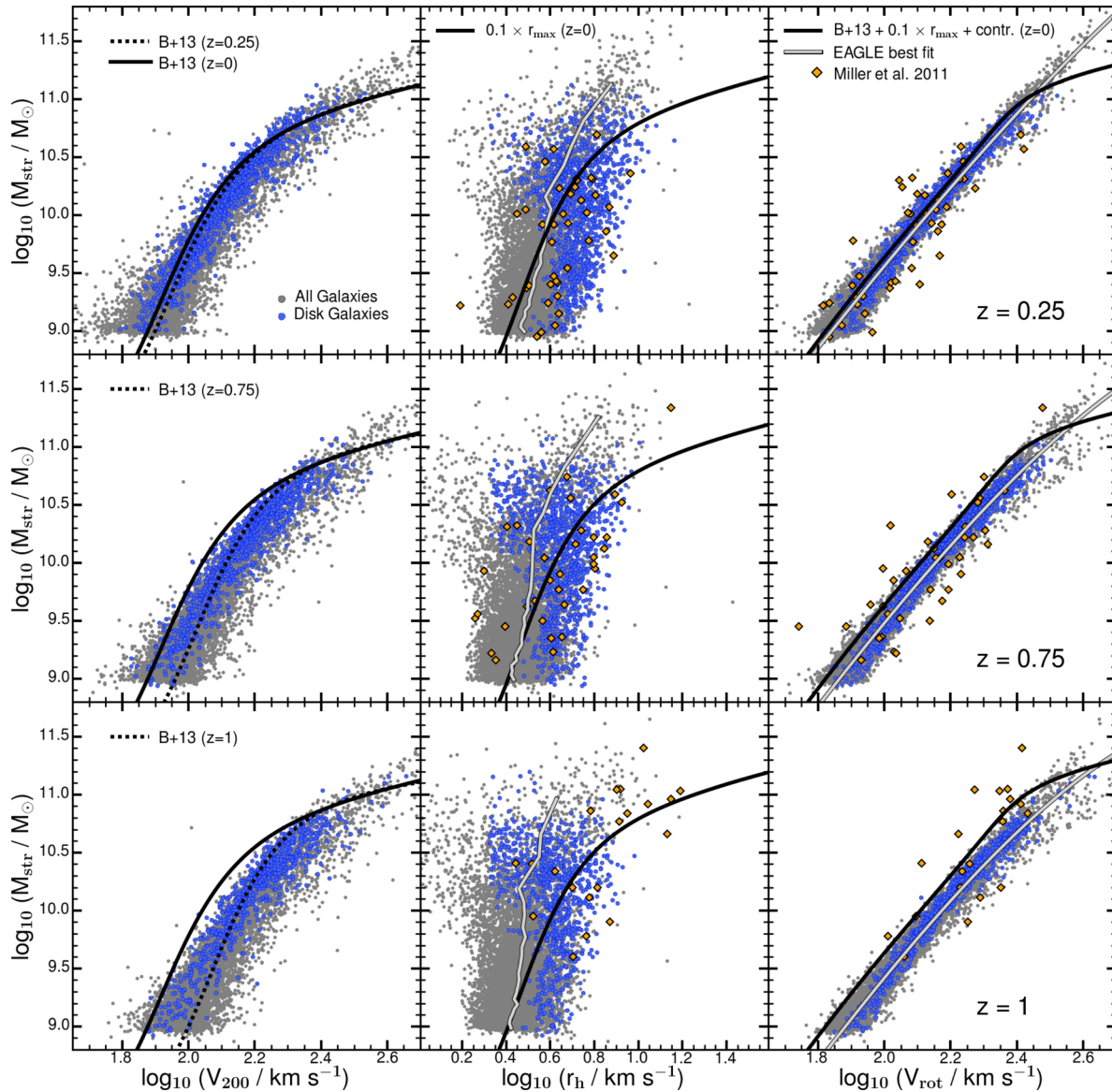
Figure 7. Evolution of the simulated TFR, compared with data from Miller et al. (2011, orange symbols). Each row is as in Fig. 3. Solid black lines in each panel are the same as in Fig. 1, and are included to aid comparison. The dotted curves in the left panels indicate the predictions from the B+13 AM model. The thin grey lines are fits to EAGLE galaxies, with parameters given in Table 1. EAGLE galaxies match the AM predictions reasonably well, as well as the size and TFR of galaxies in the observed sample at all redshifts. See text for a more in-depth discussion.

end, dropping by roughly a factor of 2 back to $z = 1$ from present values. The evolution is weaker, but still noticeable, at the low-mass end. Interestingly, the half-mass radii of simulated galaxies at early times agree fairly well with those in the Tully–Fisher samples of Miller et al. (2011). The only difference is at $z = 1$, where at the high-mass end the observed galaxies seem significantly larger than simulated galaxies of similar mass. The good match with observations is consistent with the results of Furlong et al. (2015a), who found that EAGLE reproduces the observed size evolution relatively well.

The TFR at each redshift is shown in the right-hand column of Fig. 7, and shows good agreement with the data of Miller et al. (2011). The evolution in size partly compensates for the decrease in galaxy formation efficiency at fixed virial velocity, as shown in the $z = 1$ panels of Fig. 5. This shifts galaxies closer to the $z = 0$ relation, weakening the evolution of the resulting TFR.

The exception is at $z = 1$, where observed galaxies have slightly lower velocities than in the simulation. Recalling the discussion in Section 2, the reason for the offset is most likely driven by the mismatch in galaxy sizes. At given mass, the larger the galaxy the lower the contribution of the disc to the circular velocity and the weaker the halo response, leading, on average, to lower velocities. Had our simulation produced galaxies as massive and large as those in the $z = 1$ Miller et al. (2011) sample, it is quite likely that they would have matched the observed velocities.

It is unclear at this point whether the lack of large, massive discs at $z = 1$ in EAGLE is a problem for the model or a result of the relatively small simulated volume, coupled with inherent selection biases affecting observational samples. Indeed, no such discrepancy was found by Furlong et al. (2015a), who compared EAGLE with data from van der Wel et al. (2014). Large, massive discs are obviously easier to observe at high redshift: given the sensitivity of

the TFR to galaxy size, this has the potential of inducing biases in the relation that ought to be carefully taken into account. With this caveat, we conclude that the overall TFR evolution seen in EAGLE is quite consistent with presently available observational constraints.

4 SUMMARY AND CONCLUSIONS

We have used the EAGLE set of ΛCDM cosmological hydrodynamical simulations to study the relation between AM, galaxy sizes, and the TFR. Our main findings may be summarized as follows.

(i) Galaxies that match the predictions of AM are consistent with the observed TFR despite the non-monotonic behaviour of the galaxy formation efficiency with halo mass. Consistency with the observed TFR requires galaxies to follow the mass–size relation of observed galaxy discs, and haloes to respond to galaxy assembly by contracting, roughly as predicted by simple adiabatic contraction models.

(ii) EAGLE galaxies match all of these constraints approximately, and show a TFR in good agreement with observation at $z = 0$.

(iii) Galaxy size and halo contraction induce a strong correlation between galaxy formation efficiency and rotation speed that straightens the TFR into a single power law and scatters galaxies along the main relation, keeping its dispersion tight. As a result, the scatter of the simulated TFR is substantially lower than observed, even when *all* galaxies are considered, rather than only late-type discs.

(iv) The EAGLE galaxy–halo mass relation evolves roughly as expected from AM models and its galaxy mass–size relation evolves in accord with that of galaxies in distant Tully–Fisher samples. This results in gradual but weak evolution of the simulated TFR in reasonable agreement with observed constraints, despite the more rapid evolution in galaxy formation efficiency predicted by AM models.

The sensitivity of the TFR to galaxy size explains why many simulations have argued consistency with this scaling relation while, at the same time, failing to match the galaxy masses predicted by AM models. Indeed, it is always possible to trade disc mass for galaxy size so that the resulting TFR remains nearly invariant. A galaxy formation simulation cannot therefore be considered successful unless it matches simultaneously with the TFR, as well as the abundance and size of galaxies as a function of stellar mass. Overall, our results show that the slope, zero-point, scatter, and evolution of the TFR pose no obvious difficulty to galaxy formation models in the ΛCDM cosmogony.

REFERENCES

Aaronson M., Huchra J., Mould J., 1979, ApJ, 229, 1
Abadi M. G., Navarro J. F., Steinmetz M., Eke V. R., 2003, ApJ, 597, 21
Abadi M. G., Navarro J. F., Fardal M., Babul A., Steinmetz M., 2010, MNRAS, 407, 435
Aumer M., White S. D. M., Naab T., Scannapieco C., 2013, MNRAS, 434, 3142
Avila-Reese V., Zavala J., Firmani C., Hernández-Toledo H. M., 2008, AJ, 136, 1340
Barnes J., White S. D. M., 1984, MNRAS, 211, 753
Behroozi P. S., Marchesini D., Wechsler R. H., Muzzin A., Papovich C., Stefanon M., 2013, ApJ, 777, L10 (B+13)
Bell E. F., de Jong R. S., 2001, ApJ, 550, 212
Bell E. F., McIntosh D. H., Katz N., Weinberg M. D., 2003, ApJS, 149, 289
Benitez-Llambay A., 2015, py-sphviewer: Py-SPHViewer v1.0.0. Available at: http://dx.doi.org/10.5281/zenodo.21703
Blumenthal G. R., Faber S. M., Flores R., Primack J. R., 1986, ApJ, 301, 27
Böhm A. et al., 2004, A&A, 420, 97
Brook C. B. et al., 2011, MNRAS, 415, 1051
Cattaneo A., Salucci P., Papastergis E., 2014, ApJ, 783, 66
Cole S., Lacey C. G., Baugh C. M., Frenk C. S., 2000, MNRAS, 319, 168
Conselice C. J., Bundy K., Ellis R. S., Brichmann J., Vogt N. P., Phillips A. C., 2005, ApJ, 628, 160
Courteau S., 1997, AJ, 114, 2402
Courteau S., Dutton A. A., van den Bosch F. C., MacArthur L. A., Dekel A., McIntosh D. H., Dale D. A., 2007, ApJ, 671, 203
Crain R. A. et al., 2015, MNRAS, 450, 1937
Cresci G. et al., 2009, ApJ, 697, 115
Dalla Vecchia C., Schaye J., 2012, MNRAS, 426, 140
Davis M., Efstathiou G., Frenk C. S., White S. D. M., 1985, ApJ, 292, 371
Desmond H., Wechsler R. H., 2015, MNRAS, 454, 322
Dolag K., Borgani S., Murante G., Springel V., 2009, MNRAS, 399, 497
Dutton A. A., Conroy C., van den Bosch F. C., Prada F., More S., 2010, MNRAS, 407, 2
Eke V. R., Baugh C. M., Cole S., Frenk C. S., King H. M., Peacock J. A., 2005, MNRAS, 362, 1233
Flores H., Hammer F., Puech M., Amram P., Balkowski C., 2006, A&A, 455, 107
Förster Schreiber N. M. et al., 2009, ApJ, 706, 1364
Frenk C. S., White S. D. M., Davis M., Efstathiou G., 1988, ApJ, 327, 507
Furlong M. et al., 2015a, preprint (arXiv:1510.05645)
Furlong M. et al., 2015b, MNRAS, 450, 4486
Governato F., Willman B., Mayer L., Brooks A., Stinson G., Valenzuela O., Wadsley J., Quinn T., 2007, MNRAS, 374, 1479
Guedes J., Mayer L., Carollo M., Madau P., 2013, ApJ, 772, 36
Guo Q., White S., Li C., Boylan-Kolchin M., 2010, MNRAS, 404, 1111
Gurovich S., Freeman K., Jerjen H., Staveley-Smith L., Puerari I., 2010, AJ, 140, 663
Haynes M. P., Giovanelli R., Chamaraux P., da Costa L. N., Freudling W., Salzer J. J., Wegner G., 1999, AJ, 117, 2039
Kassin S. A. et al., 2012, ApJ, 758, 106
Lacey C. G. et al., 2016, MNRAS, 462, 3854
Ludlow A. D., Bose S., Angulo R. E., Wang L., Hellwing W. A., Navarro J. F., Cole S., Frenk C. S., 2016, MNRAS, 460, 1214
McCarthy I. G., Font A. S., Crain R. A., Deason A. J., Schaye J., Theuns T., 2012, MNRAS, 420, 2245
Marinacci F., Pakmor R., Springel V., 2014, MNRAS, 437, 1750
Mathewson D. S., Ford V. L., Buchhorn M., 1992, ApJS, 81, 413

Miller S. H., Bundy K., Sullivan M., Ellis R. S., Treu T., 2011, ApJ, 741, 115

Mo H. J., Mao S., White S. D. M., 1998, MNRAS, 295, 319

Moster B. P., Naab T., White S. D. M., 2013, MNRAS, 428, 3121

Navarro J. F., Steinmetz M., 2000, ApJ, 538, 477

Navarro J. F., Frenk C. S., White S. D. M., 1996, ApJ, 462, 563

Navarro J. F., Frenk C. S., White S. D. M., 1997, ApJ, 490, 493

Okamoto T., Eke V. R., Frenk C. S., Jenkins A., 2005, MNRAS, 363, 1299

Pizagno J. et al., 2007, AJ, 134, 945 (P+07)

Planck Collaboration I, 2014, A&A, 571, A1

Reyes R., Mandelbaum R., Gunn J. E., Pizagno J., Lackner C. N., 2011, MNRAS, 417, 2347

Rosas-Guevara Y. M. et al., 2015, MNRAS, 454, 1038

Sales L. V., Navarro J. F., Theuns T., Schaye J., White S. D. M., Frenk C. S., Crain R. A., Dalla Vecchia C., 2012, MNRAS, 423, 1544

Sales L. V. et al., 2016, preprint (arXiv:1602.02155)

Sawala T., Frenk C. S., Crain R. A., Jenkins A., Schaye J., Theuns T., Zavala J., 2013, MNRAS, 431, 1366

Sawala T. et al., 2015, MNRAS, 448, 2941

Scannapieco C. et al., 2012, MNRAS, 423, 1726

Schaller M. et al., 2015a, MNRAS, 451, 1247

Schaller M., Dalla Vecchia C., Schaye J., Bower R. G., Theuns T., Crain R. A., Furlong M., McCarthy I. G., 2015b, MNRAS, 454, 2277

Schaye J., Dalla Vecchia C., 2008, MNRAS, 383, 1210

Schaye J. et al., 2015, MNRAS, 446, 521

Springel V., 2005, MNRAS, 364, 1105

Springel V., Yoshida N., White S. D. M., 2001, New Astron., 6, 79

Steinmetz M., Navarro J. F., 1999, ApJ, 513, 555

Torrey P., Vogelsberger M., Genel S., Sijacki D., Springel V., Hernquist L., 2014, MNRAS, 438, 1985

Tully R. B., Fisher J. R., 1977, A&A, 54, 661

Tully R. B., Pierce M. J., Huang J.-S., Saunders W., Verheijen M. A. W., Witchalls P. L., 1998, AJ, 115, 2264

Vale A., Ostriker J. P., 2004, MNRAS, 353, 189

van der Wel A. et al., 2014, ApJ, 788, 28

Verheijen M. A. W., 2001, ApJ, 563, 694

Vogelsberger M., Genel S., Sijacki D., Torrey P., Springel V., Hernquist L., 2013, MNRAS, 436, 3031

Wiersma R. P. C., Schaye J., Smith B. D., 2009a, MNRAS, 393, 99

Wiersma R. P. C., Schaye J., Theuns T., Dalla Vecchia C., Tornatore L., 2009b, MNRAS, 399, 574

Williams M. J., Bureau M., Cappellari M., 2010, MNRAS, 409, 1330

Ziegler B. L. et al., 2002, ApJ, 564, L69

This paper has been typeset from a TEX/LATEX file prepared by the author.